

Video camera and seismic monitoring of water bulge explosion at Strokkur Geyser, Iceland

✉ Eva P. S. Eibl*^α,  Sandeep Karmacharya^α,  Alina V. Shevchenko^β,  Thomas R. Walter^β, and  Gylfi Páll Hersir^γ

^α University of Potsdam, Institute of Geosciences, Karl-Liebknecht-Str. 24/25, 14467 Potsdam, Germany.

^β GFZ - German Research Center for Geosciences, Potsdam, Germany.

^γ Independent Researcher, Reykjavík, Iceland.

ABSTRACT

Eruptions of volcanoes and geysers share many fundamental similarities: for example, they are manifestations of Earth's geothermal energy, involving the pressure-driven expulsion of fluids from the Earth's interior. However, while volcanoes can produce spectacular lava bubbles that burst, water bubbles are rarely observed on the surface of geysers. It is still unclear why some of these low-viscosity geyser systems produce none, while others produce them regularly. There is no quantification of the size, speed, and height of these bubbles at geysers, which is the gap we fill here. Strokkur creates a water bulge in its surface pool (bulge stage). When the bulge bursts, water is ejected into the air (jet stage). The steam then continues to rise buoyantly and drift away (drift stage). Here we study the evolution of the three stages using records from video camera campaigns and a local seismic network. We find that larger bulges are associated with larger ascent velocities and cause larger jet heights. As energy is channeled into a high jet, small seismic ground motions are recorded. The bulge formation itself is barely visible seismically. Our work suggests that the 0.74 ± 0.27 s-long bulge stage can be used as a first-order proxy for predicting eruption height. This study might also be relevant for understanding fluid dynamics in volcanic systems.

KEYWORDS: Geyser; Iceland; Seismometer; Video camera; Bubble explosion; Water jet.

1 INTRODUCTION

Bubbles that rise, push the fluid surface into a bulge and burst, are spectacular and often reported features of silicic eruptions [Vergnolle and Brandeis 1996; Bouche et al. 2010; Eibl et al. 2023]. For lower viscosity lavas, the same is observed at carbonatite volcanoes [Keller and Krafft 1990] or mud volcanoes [Hovland et al. 1997; Edwards et al. 2017]. However, at the lower end of the viscosity scale at geysers, bubbles that push the fluid surface into a bulge before bursting are rarely reported [Bryan 2008]. Some geysers have no record of this, and at others, such as Great Fountain, USA, they occur from time to time. At Great Geysir, Iceland, bulges occur only at the very beginning of a several-minute-long eruptive sequence, characterized by an initially vapor-rich eruption which becomes progressively water-rich, draining the water from the pool and conduit. On a smaller and more irregular scale, other geysers produce bulges in the El Tatio geyser field (Chile) and in the Geyser Valley (Kamchatka). Finally, they occur regularly at the Strokkur geyser in Iceland. It is not yet known why geysers behave so differently, and a quantification and assessment of the bulge formation at geysers is lacking.

Geysers periodically erupt water into the air. Maintaining this spectacle requires a delicate balance of water supply, a heat supply, a fracture system, and a conduit [Descloizeaux 1847] and as such they are similar to volcanoes. There are less than 1000 geysers worldwide [Hurwitz and Shelly 2017]. However, geysers are important in a variety of research areas, ranging from climate change to the origin of life and mineral deposits [Hurwitz et al. 2021].

On the surface, these geysers can form either a cone or a pool of hydrothermal fluid, known to control cooling and dynamics of the system [Hurwitz and Manga 2017]. Moreover, the eruption interval, water and steam volume, eruption height, and coupling to the environment all depend on the structure at depth, in particular the location, shape, presence or absence of underground reservoirs, the size of a conduit, heat input from depth, and water mixing conditions [MacKenzie 1811; Bunsen 1847; Nishimura et al. 2006; Quezada-Reyes 2012; Karlstrom et al. 2013; Munoz-Saez et al. 2015; Eibl et al. 2020a; 2021; Reed et al. 2021]. In general, two competing models have been proposed for driving geyser eruptions: (i) Geysers are driven by steam that accumulates in a bubble trap beneath the geyser [MacKenzie 1811]. This setup allows in theory hot and cold geysers driven by water steam, CO₂ or other gases. (ii) Geysers contain superheated water in a conduit that moves upward and turns to steam during the eruption [Bunsen 1847].

Methods that provide high temporal resolution facilitate our understanding of processes at depth. For example, infrasound signals compared to video cameras have been used at some Yellowstone geysers to infer the pressure field during eruptions [Quezada-Reyes 2012]. Pressure and temperature sensors have been used to study recharge and discharge processes [Hutchinson et al. 1997; Collignon et al. 2023]. For example, multidisciplinary studies have used tiltmeters, acoustic sensors, flow pressure sensors, and temperature sensors to infer that boiling due to pressurization drives Onikobe Geyser, Japan [Nishimura et al. 2006]. This knowledge is crucial, for example, to improve the conceptual models of geysers, but our hypothesis and models still cannot explain all the observed features of a geyser, especially the explosion timing and the

*✉ eva.eibl@uni-potsdam.de

eruption heights, which are often thought to be difficult to predict.

In general, video camera data can aid in the interpretation of seismic or acoustic data. Thus, seismic or acoustic data and video cameras are often combined in volcanic [Alparone et al. 2003; Eibl et al. 2023] or geyser contexts [Quezada-Reyes 2012; Karlstrom et al. 2013; Eibl et al. 2021]. After the first multidisciplinary phase, in which the interpretation of the data can be established, the number of different sensor types in a network can be reduced to limit maintenance costs in the field.

A seismometer or microphone could then be used alone to track the geyser's behavior over the long term. Video camera data can be used alone in the short term at other geysers to measure parameters that provide insight into the structure at depth [Karlstrom et al. 2013; Munoz-Saez et al. 2015]. For example, a recent idea proposed by Reed et al. [2021] is to use the height of the geyser fountain to directly infer the depth of the bubble trap based on an apparently linear relationship. Conversely, a relationship between seismic amplitudes and geyser fountain heights could be used to estimate geyser fountain heights in the long term, when high temporal resolution video camera data are not available but seismic data are.

Similar approaches have been used at volcano observatories, e.g. in Kamchatka, Mexico, Spain, and elsewhere. However, despite several studies comparing volcanic eruption height and seismic amplitude, some find a correlation [Koyanagi et al. 1987; McNutt 1987; Alparone et al. 2003] while others do not [Tanguy and Patané 1984; Eibl et al. 2023] or even report an anti-correlation [Privitera et al. 2003]. Such a relationship has not yet been investigated for geysers.

To establish a link between video camera and seismic data, we instrumented Strokkur geyser in Iceland in June 2017, March 2020, and August 2022 (Section 2). We analyze video camera and seismic data (Section 3) to study the blue bulge that forms due to the rising steam bubble before eruptions and derive its height and rising velocity until it bursts (Section 4.1 and 4.2) and compare the bulge formation to the seismic amplitudes (Section 4.3). We repeat these steps to derive the fountain height and velocity (Section 4.4 and 4.5), and compare the height to the seismic amplitude (Section 4.6). Finally, we discuss limitations (Section 5.1) and implications of this work.

2 STUDY AREA AND FIELD CAMPAIGNS

Strokkur is a geyser in the Haukadalur valley and is one of the main tourist attractions in SW Iceland. The heat beneath Strokkur comes from a geothermal reservoir of an Upper Pleistocene volcano [Jones et al. 2007]. The geyser and the hot springs in the valley have formed several solid sinter terraces that are interspersed with soil and vegetation (Figure 1) [Barth 1940].

Strokkur hosts a water-filled pool on the surface with a diameter of 7–8 m. Based on our orthophoto from 2018 the pool had a size of 58.7 m². Most likely, dissolved CO₂ has always been in the water from Strokkur like the other hot springs in the geyser area [Arnórs-son 1985; Pasvanoglu 1998; Pasvanoglu et al. 2000]. There are remnants of a square construction wall visible approximately 3 × 3 m, which was made for stabi-

lization during the drilling operation in 1963. The shallow conduit is nearly circular with a diameter of 2 m near the surface, becomes more elliptical at a depth of ~12 m, and narrows further at a depth of ~20 m at artificial boreholes [Walter et al. 2020]. The conduit also has a sintered rim, that is partly visible above the water. The outline of the rim is elongated and reaches a maximum width of 3.1 m. We measured the rim width (perpendicular to the line of sight of the 2020 camera) on the georeferenced orthophoto (Figure 1) to validate the images scaling using the pole (Figure S1) and thus to validate our bulge height measurements.

Strokkur has been a tourist attraction for centuries, but early scientific studies of its history and structure are rare. According to the travel books of Sveinn Pálsson, the first university-educated nature scientist in Iceland [Pálsson 1983], Strokkur was blocked in 1708 as people threw stones and turf into the pool. Pálsson's detailed descriptions go back to 1793 when he gave Strokkur its name and estimated the eruption height to be more than 50 m and a transition from a water fountain to a steam fountain during an eruption. After the earthquake(s) in 1789 Strokkur became active again. Eruptions were not frequent but they were powerful.

The activity of Strokkur began to decline after 1830, when people threw stones and turf into the pool to provoke an eruption—these eruptions were described as being only 20 m high and very muddy [Pálsson 1983]. After the earthquake in September 1896, eruptions stopped. Strokkur started erupting again in 1907, featuring only small eruptions and stopped completely in 1920. Short reactivations by adding soap to the system had no long term effect on the geysers [Rinehart 1968]. A 39.4 m-deep well was drilled in Strokkur in July 1963 to clean the pipe and the geyser has been active since then, the only inflow being at the bottom of the well [Torfason 1995].

A scientific measurement of Strokkur's eruption was made in 1804 [Ohlsen 1805]. While carrying out geodetic measurements for the Danish government in the southern lowlands, Ohlsen measured a fountain height of 45 m for Strokkur. When Strokkur had finished the water eruption, it erupted steam for 2 hours [Ohlsen 1805]. A connection between the eruptions at Strokkur and at the Great Geysir (about 130 m to the NE) was documented at that time.

The total outflow from the geyser area was 14 to 15 L s⁻¹ in 1967, including 2.5 L s⁻¹ from Strokkur [Ólafsson 1967]. According to Torfason [1995] the total outflow in 1994 had decreased to 9 to 9.5 L s⁻¹ and at Strokkur to 2.1 to 2.3 L s⁻¹. It was also estimated that Strokkur erupted every seven minutes in 1994 (nine eruptions per hour). The temperature in the reservoir based on geothermometry was 230 to 250°C [Arnórs-son 1985].

Nowadays, Strokkur is characterized by single eruptions and multi-tuple eruptions. Multi-tuple means that two or more eruptions occur close together in time, followed by a longer waiting period. At Strokkur, our previous work has shown that single to sextuple eruptions occur, consisting of one to six fountains with an average spacing of 16.1 s [Eibl et al. 2020a]. As the number of fountains increases, the waiting time between eruptions increases linearly from 3.7±0.9 to 16.4 min [Eibl et al. 2020a]. The geyser goes through certain stages

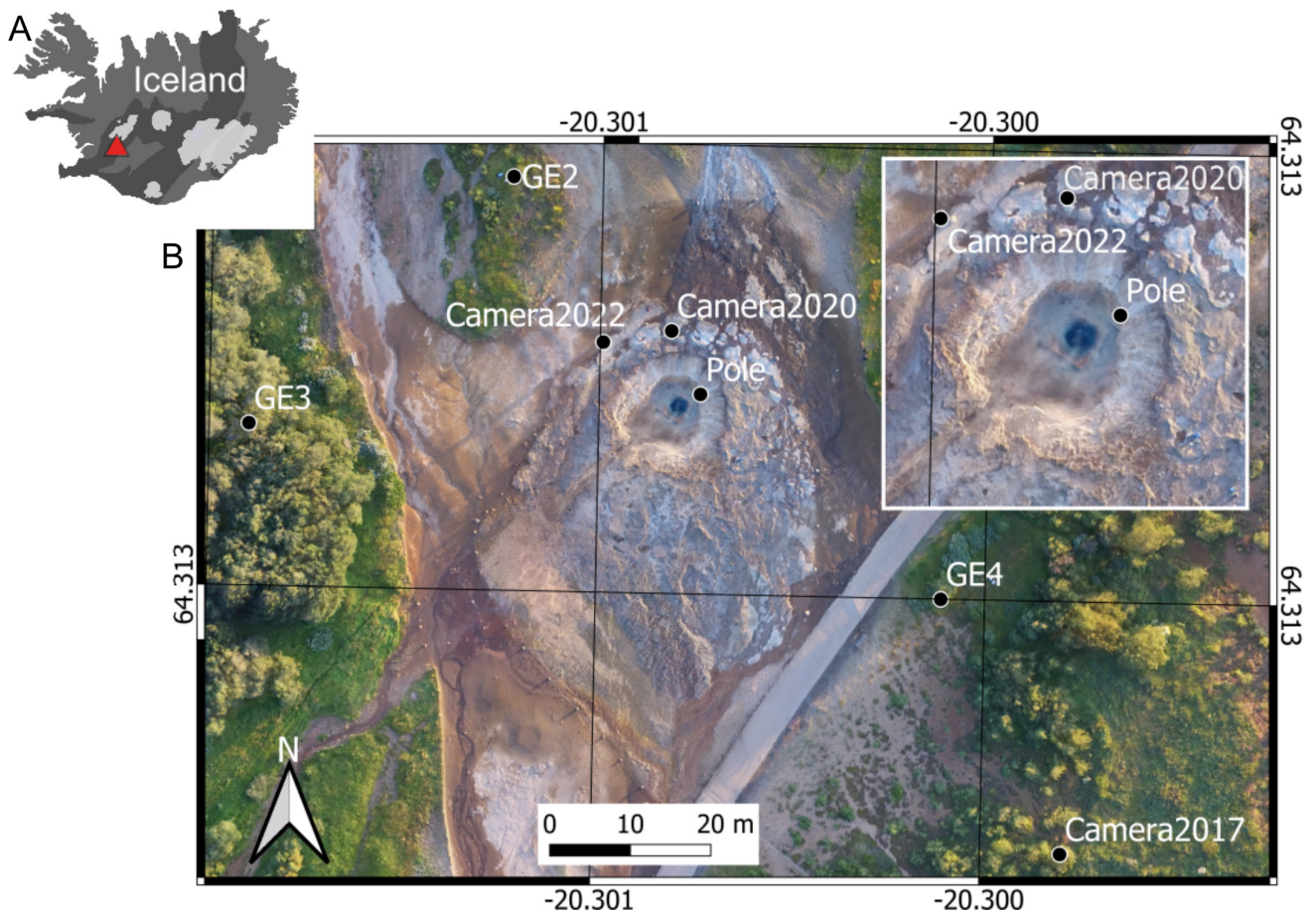


Figure 1: Overview of the seismic and video camera network near Strokkur geyser. [A] Location of Strokkur in Iceland. [B] Drone-based orthophoto from 2018. Seismometers GE2 to GE4 recorded from 9 to 15 March 2020. Camera locations named according to the year. Camera2020 recorded the bulge growth on 13 and 14 March 2020, Camera2017 from 27 to 30 June 2017 and Camera2022 on 16 August 2022. The location of our reference pole is marked. The inset shows the hydrothermal pool and conduit of Strokkur.

within an eruptive cycle: During stage (i), an eruption ejects a fountain of water into the air. During stage (ii), water refills the conduit. During stage (iii) the bubble accumulates in a reservoir at about 23.7 ± 4.4 m depth 13 to 23 m west of the conduit, and during stage (iv) regular bubble collapses occur at shallow depth in the conduit [Eibl et al. 2021].

Here, we investigate stage (i) in further detail. We subdivide this stage into three sub-stages. An eruption starts when a steam bubble reaches the water surface (Figure 2A). As the bubble rises in the conduit, it pushes up the water surface above the conduit. Most of the water surface in the pool remains flat. This bulge initially appears blue (Figure 2B), grows in height, and turns white as steam arrives from depths and water evaporates into steam. We refer to this as the **bulge stage**. When the surface of the water bulge finally bursts at one point, it breaks at several other points within a fraction of a second (Figure 2C). This results in a jet of water (Figure 2D) and marks the transition from the bulge stage to the **jet stage**. Finally, in the **drift stage** water drifts away (Table 1). We explore whether the size of the water bulge allows foretelling the strength and height of the next eruption.

3 DATA AND METHODS

3.1 Experimental setup 2017, 2020, and 2022

During three fieldwork campaigns in 2017, 2020, and 2022 we recorded bulge growth videos.

- From 27 to 30 June 2017, a Nikon D7000 was placed at a distance of 70 m to the southeast of the pool to record the fountain height (Figure 1). The camera recorded video files at 1920×1080 pixels with a temporal resolution of 50 fps (frames per second). To estimate the jet and drift height a lower temporal resolution was used to extract frames to speed up the processing time. We reduced camera shake by using a stable tripod with a height of 50 cm above ground. The camera has an internal timer, and is further time-synchronized by holding a GPS timer in front of the lens at the beginning and ending of each video.

- From 13 to 14 March 2020, two SONY DSC-RX100M3 cameras were used to record the bulge growth (Figure 1). The cameras were mounted on a tripod about 0.8 m above the ground. The cameras were about 10 m from the conduit and recorded at 1920×1080 pixels at a frame rate of 25 fps. Bulge

Table 1: Overview and definition of terms used in manuscript.

Term	Definition
Bulge stage	Water surface is pushed upwards into a water bulge (Figure 2B)
Jet stage	Water jets into the air and falls on the ground (Figure 2D)
Drift stage	Dispersed water drifts away and falls on the ground
Pulse	One jet can be composed of several pulses
Fountain	Contains jet and drift stage
Eruption	Contains one or several cycles of bulge, jet and drift stage
Phase (i) in Eibl et al. [2021]	Mainly jet stage and seismically noisy part of bulge and drift stage
Single eruption in Eibl et al. [2020a]	Features one water fountain followed by a mean waiting time of 3.7 ± 0.9 min until the next eruption
Double eruption in Eibl et al. [2020a]	Features two water fountains at an average spacing of 16.1 ± 4.8 s followed by a mean waiting time of 6.2 ± 1.3 min until the next eruption

growth was recorded for 30 min on 13 March from 18:43 to 19:12 and for 27 min on 14 March from 16:55 to 17:22. In 2020 we recorded nine single eruptions and one double eruption on 13 March and six single eruptions and one double eruption on 14 March.

- On 16 August 2022, we used a Nikon P7100 camera mounted on a tripod at a height of about 1 m. We recorded the bulge formation from 20:50 to 22:15, placing the camera at a distance of about 12 m from the conduit, in three videos of about 25 to 30 min each. The videos had a resolution of 1280×720 pixels and a frame rate of 30 fps. We recorded 22 bulges from 16 single eruptions and four double eruptions (where two first water fountains were not recorded).

The different cameras, viewing geometries, sensors, lenses and resolutions result in a pixel to meter conversion for each record as described below.

We use reference distances to scale lines of pixels to meters. During the year 2017, we used the height of a colleague (175 cm) as a point of reference while she was standing directly next to Strokkur. Through this, we determined a pixel-to-meter ratio of 25.14 pixels per meter (i.e. a pixel resolution of 4 cm).

In the year 2020, we used different methods to determine the pixel-to-meter ratio near the conduit. On 14 March, we utilized a vertical pole measuring 1.8 m in length (as depicted in Figure S1) to calculate this ratio. The resulting pixel-to-meter value was 116.681 pixels per meter (i.e. 1 px is ~ 0.9 cm). On 13 March, we utilized a high-resolution orthophoto to obtain the width of the conduit rim. This width was then set as the reference scale on the video frame, considering the partially visible portion above the water. This approach yielded a pixel-to-meter ratio of 107.126 pixels per meter (i.e. 1 px is ~ 0.93 cm).

For the purpose of calculating the bulge and eruption height in the year 2022, we utilized another person's height as a reference, which was measured at 168 cm. By employing this reference, we determined a pixel-to-meter ratio of 89.285 pixels per meter (i.e. the pixel resolution is 1.12 cm) for the video data recorded in August 2022.

3.2 Image processing methods

3.2.1 Image extraction and kymograph

We extract the image frames from the video using the FFmpeg plugin, a leading multimedia framework for decoding and filtering image data (git, v 4.3). Images were extracted at 5 frames per second for 2017, 25 frames per second for 2020, and 30 frames per second for 2022.

The analysis of the 2017 camera data involves utilizing a kymograph recording technique, which has been previously employed in studying geysers [Namiki et al. 2014; Munoz-Saez et al. 2015]. To generate the kymograph, we treat the video as a collection of image data. Specifically, we choose a vertical line of pixels positioned above the center of the geyser conduit across all images, and we plot the color values of these pixels along a time axis. By examining this time-space plot at Strokkur, we can identify the timing, height, and duration of eruptions as depicted in the camera images. To verify whether the frequency and seismic amplitude measurements correspond to the eruption height, we compare the kymograph with independent seismic observations.

3.2.2 Height and velocity estimation

We imported the extracted images to ImageJ (v 1.53c) [Schindelin et al. 2012] to create image stack data. MTrackJ (v 1.5.1) [Meijering et al. 2012] was used to track bulge formation/growth and eruption height.

For the 2017 data, we considered the ground that is vertically below the top point of the fountain visible in the video data as a base point to calculate the fountain height. The top part of the steam plume coming off the jet was measured during the drift phase, as the droplets were not clearly visible. For data from 2020 and 2022, we chose a fixed base point based on the unique topography visible in the data.

Using 2017 data, we only calculated the eruption jet height and drift height as it was located far from the Geyser and no bulge formation was visible. Using March 2020 and August 2022 data, we only derived the bulge height since the camera is located too close to the pool to capture the whole jet height.

For comparison, we used a Sobel edge detection algorithm [Zhang et al. 2009] on the same data stack to estimate the foun-

tain height. As the fountain height is well-defined during the jet stage, the maximum jet height could be determined.

For 2020 and 2022 data, the rising velocity of the bulge is calculated using: $s = d/t$ where d is the vertical distance covered between one frame and the next, and t is the time needed to cover the distance.

3.2.3 Volume estimation

We calculate the maximum bulge volume before the outburst for a bulge on 14 March. We measure the base (3.4 m) and height (h) (0.7 m) of the bulge in the image (Figure S1B). By approximation of a circle, which corresponds to the bulge's outline in the upper part, we obtain the radius (R) of the circle, allowing us to calculate the volume of the subaerial part of the bulge.

3.3 Seismometer Data Processing

We compare the camera-derived data to independent seismometer data. We use data from a seismic network which is at the same location as the 7L network in 2017/18 [Eibl et al. 2020b]. Three seismometers are at 38.8 m (G4, SE), 42.5 m (G2, NNW) and 47.3 m (G3, SW) from the center of Strokkur. We derive an eruption catalogue following the approach by Eibl et al. [2020a] using the Pyrocko trace-viewer Snuffler [Heimann et al. 2017] in a frequency band from 5 to 25 Hz. The 2020 eruption times derived using the video cameras are consistent with the eruption times in the seismic catalogue.

We use data from seismometer G2. We detrend, taper, and instrument correct the data before filtering them using an acausal, zero-phase Butterworth bandpass filter of order 4 to the frequency band from 3 to 30 Hz. We calculate RMS values in 1 s-long time windows and 50 % overlap.

We use the 3 component seismometer data to derive the maximum seismic amplitude in ground velocity. We calculate the root of the sum of the squared components. To extract the matching RMS seismic amplitude for the derived heights from video camera data, we require a time deviation of less than 0.3 s. For the comparison with eruption height, we squared the RMS amplitude to estimate the seismic energy.

4 RESULTS

4.1 Stacked bulge heights and rising velocities

We evaluate 19 bulges recorded by Camera2020 and 22 bulges recorded by Camera2022. All 41 bulges reach a mean width at the base of 2.65 ± 0.86 m and range from 1.03 m to 3.85 m width (Figure S1). They contain an average volume of 2.3 ± 1.7 m³ that ranges from 0.13 to 7.08 m³.

All 41 bulges reach an average height of 0.62 ± 0.18 m in the frame before the bulge bursts (Figure 2F) and 0.82 ± 0.29 m in the frame after the bulge bursts (Figure 2G). The height often increases exponentially. However, in 4 eruptions the bulge height reaches only 0.23 to 0.3 m in height before bursting and follows a more linear trend (Figure 2E). At the other extreme, 4 eruptions reach bulge heights between 0.88 and 1.1 m before bursting. The bulge height is related to the rate at which the bulge rises when it bursts: Larger bulges grow faster as they burst, while small bulges grow slower as they burst (Fig-

ure 2K and L). For example, the velocity reaches a maximum of 4.2 m s⁻¹ during the formation of the third largest bulge of 0.91 m height, which forms in 0.8 s on 13 March 2020.

The bulge rises with an average velocity of 0.9 ± 0.5 m s⁻¹ about 0.24 s before the bulge bursts (Figure 2H). This increases to an average velocity of 2.3 ± 1.1 m s⁻¹ in the frame before the bulge bursts (Figure 2I). One frame after the burst it reaches an average velocity of 4.85 ± 3.18 m s⁻¹ (Figure 2J). The bulge rising velocity increases faster than exponentially. The 4 smallest bulges rise at a velocity of 0.65 to 1.0 m s⁻¹ in the pre-burst frame, and the 5 largest bulges rise at a velocity of 3.3 to 4.2 m s⁻¹. We conclude that larger bulges are also associated with larger jet rising velocities in the jet stage.

4.2 Bulges of single and double eruptions

We separately stack the bulge heights and ascent velocities of all 31 single eruptions, six first bulges of the double eruptions, and four second bulges of the double eruptions (Figure 3). The single eruptions include both the smallest and the largest bulges, and thus show the greatest variation (Figure 3A).

For double eruptions, two second bulges were too small to measure, and three bulges were smaller than the first. Only one second bulge was larger than the first (Figure 3B and C, E, and F). In three cases, the first bulge of a double eruption was comparable to the highest bulges of single eruptions. Similarly, in three instances the first bulge of a double eruption was comparable to the intermediate bulge height of single eruptions. (Figure 3A and B). Thus, we could not identify a clear pattern between bulge height or velocity that might indicate a multi-tuple eruption. However, eruptions forming bulges with heights less than 0.35 m and velocities less than 1 m s⁻¹ are unlikely to become double eruptions.

4.3 Bulge height and rising velocity in comparison to seismic amplitude

For the comparison with the seismic data, we used only 11 bulges from 13 March 2020, which have the highest temporal accuracy. The blue bulge forms on average in 0.74 ± 0.27 s (Figure 4A). The height increase of large bulges is measured up to 1.28 s. Bulges that burst at smaller heights can only be measured for less than 0.5 s. Within this time window, the height increases steadily (Figure 4A).

The velocity generally increases towards the time of bulge burst (Figure 4B). However, on a smaller scale, the velocity reaches several local minima on the way to the maximum observed bulge rise velocity.

For each time window in which we measure the bulge height and velocity, we extract the associated seismic amplitude (Figure 4C). Since bulges do not always burst at the same location the seismic energy is not always strongest on the same component. We therefore compare the bulge properties with the maximum seismic amplitude (black line in Figure 4C). The maximum seismic amplitude increases slightly towards the eruption for 6 of the 11 bulges. For all others, there is no clear relation to bulge velocity or height.

The largest bulges are accompanied by small peak seismic amplitudes and a medium-high velocity. The largest seismic amplitude is recorded during a medium-high bulge, and the

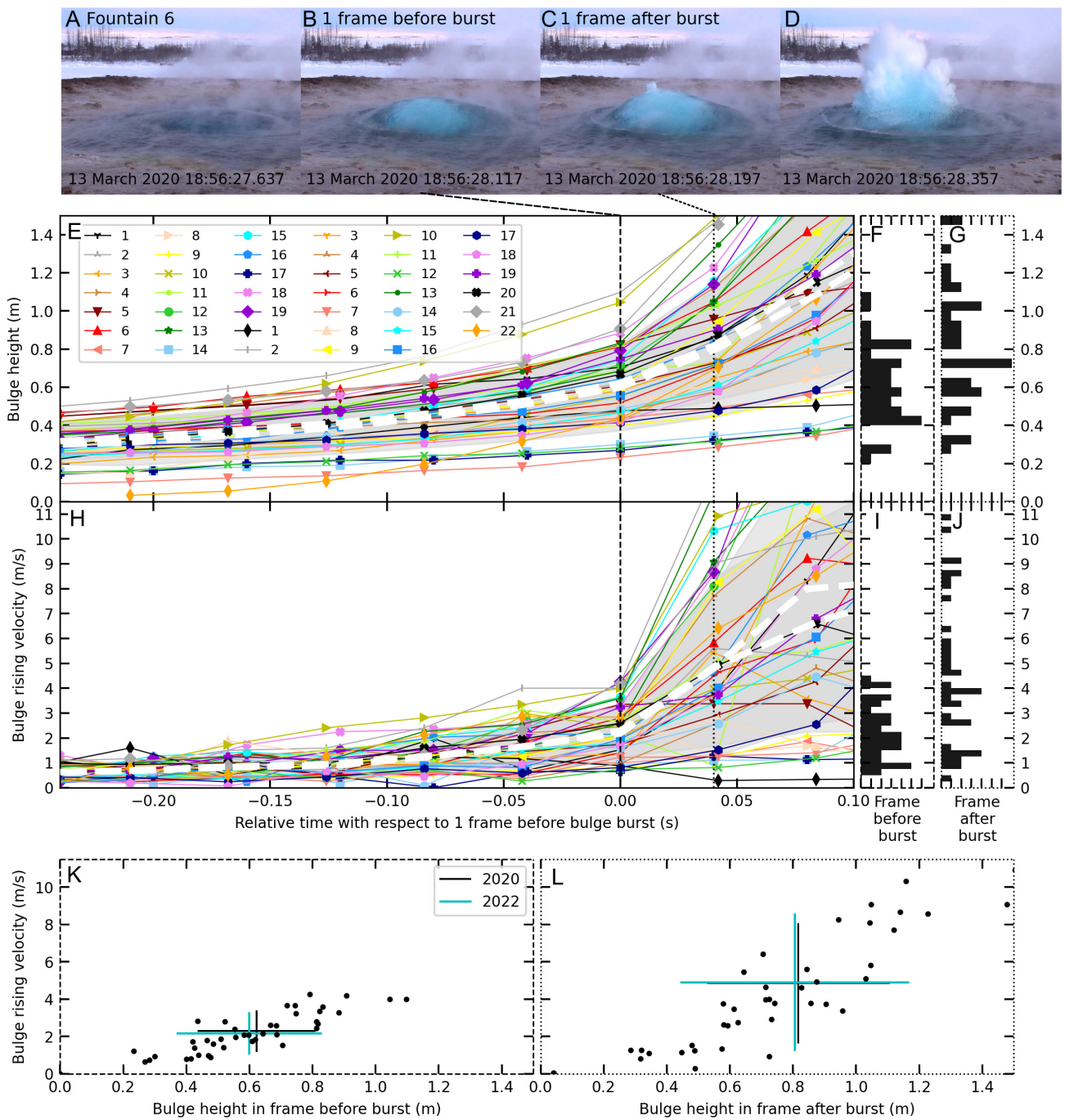


Figure 2: Evolution of velocity and height of 19 bulges in 2020 and 22 bulges in 2022. [A] The water surface is pushed upwards, [B] the bulge reaches maximum height before rupture, [C] 1 frame after the rupture of the bulge and [D] the evolving water jet. [E–J] Time window from 0.24 s before to 0.10 s after the last frame before the bulge ruptures. Our measurement in this time window is more reliable than at more than 0.24 s before the bulge burst. [E] Temporal evolution of bulge height and [F] histograms of bulge height in the frame before the burst and [G] after the burst. [H] Temporal evolution of bulge rising velocity and [I] histograms of bulge rising velocity in the frame before the burst and [J] after the burst. The two white dashed lines indicate the mean in 2020 and 2022 and the grey shaded areas the respective mean ± 1 standard deviation. Note that there are two means as the temporal sampling rates were different in 2020 and 2022 and there are two shades of grey as the two grey shaded areas partly overlap. Uncertainty bars are smaller than the symbol used. [K–L] Bulge height vs. bulge rising velocity in [K] the last frame before the burst and [L] one frame after the burst. Mean values ± 1 standard deviation are highlighted for 2020 (black bars) and 2022 (cyan bars).

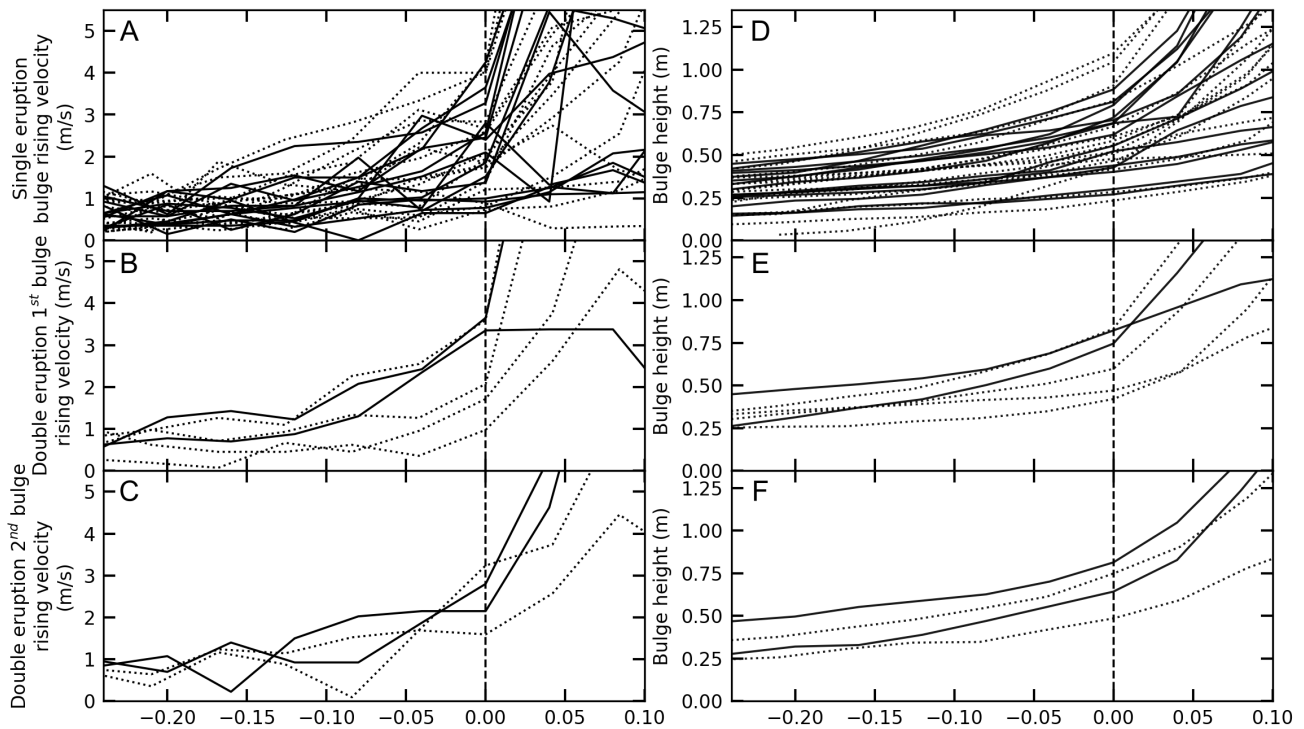


Figure 3: Bulge formation during single and double eruptions in 2020 (solid) and 2022 (dotted) relative to the frame before the bulge bursts. [A]–[C] Bulge rising velocity for [A] single eruptions, [B] first and [C] second bulge in double eruptions. The vertical dashed line marks the frame before the burst. [D]–[F] Bulge height for [D] single eruptions, [E] first bulge, and [F] second bulge in double eruptions. Note that two other second bulges were too small to determine their height.

smallest bulge causes the second largest seismic amplitude. We conclude that there is no clear trend in the recorded peak seismic amplitude and bulge height.

During bulge formation and burst the most ground motion is recorded in the north-south direction. The least ground motion is detected on the vertical components (Figure 4C). This is reasonable for a near-surface explosive source as suggested based on source locations of [Eibl et al. 2021].

4.4 Stacked jet and drift heights and velocities

From 27 to 30 June 2017, we recorded 67 water fountains in 52 single eruptions and 9 double eruptions (one first and two second fountains in a double eruption are not captured on video). For 54 of these fountains we were able to reliably determine the drift height. We separate the water rising stage into a jet stage (Figure 5A) and a drift stage (Figure 5B) and align the height and velocity time series at the time of maximum jet height.

After the bulge burst, the jet height increases rapidly for the first 1.6 s and more slowly for the next 1.2 s. The water rises from the bulge to the maximum jet height in an average of 2.8 s. However, this jet stage is as short as 1 s and as long as 3 s. The jet reaches an average height of 21.4 ± 10.2 m with a minimum height of 5.5 m and a maximum height of 42.8 m (Figure 5C and E).

Following this jet stage, the water reaches a mean observed drift height of 23.4 ± 9.5 m 2 s after the maximum jet height (Figure 5C and F). We observe minimum and maximum drift

heights of 9.6 and 46.8 m, respectively. This drift stage is characterized by a linear increase in height.

During the first about 1.6 s after the bulge bursts, the jet velocities increase. The water rises with a maximum average velocity of 14.0 ± 7.5 m s⁻¹, while the maximum jet velocities range from 1 m s⁻¹ to 44 m s⁻¹ (Figure 5D and G). This maximum velocity is reached on average within 1.6 s, which is about halfway between the bulge burst and the maximum jet height. Close to the maximum jet height the average velocities have decreased to 4.6 ± 2.1 m s⁻¹. During the drift stage, the ascent velocity is stable and averages 2.0 ± 1.0 m s⁻¹ 2 s after the maximum jet height (Figure 5D and H). For all observed eruptions the drift velocity is in the range of 0.5 to 4.5 m s⁻¹.

Note that some jets have two peaks in velocity and two rapid increases in height (e.g. number 52 in Figure 5). This indicates that some water jets are actually composed of multiple pulses, possibly caused by multiple or more complexly shaped bubbles (see work by Collignon et al. [2023] for more detail on pulses).

The six largest jet velocities exceed 28 m s⁻¹. These result in five of the six largest maximum jet heights exceeding 35 m (Figure 5I). Since larger bulges were also associated with larger bulge ascent velocities and jet velocities, we conclude that larger bulges lead to larger jet heights during eruptions.

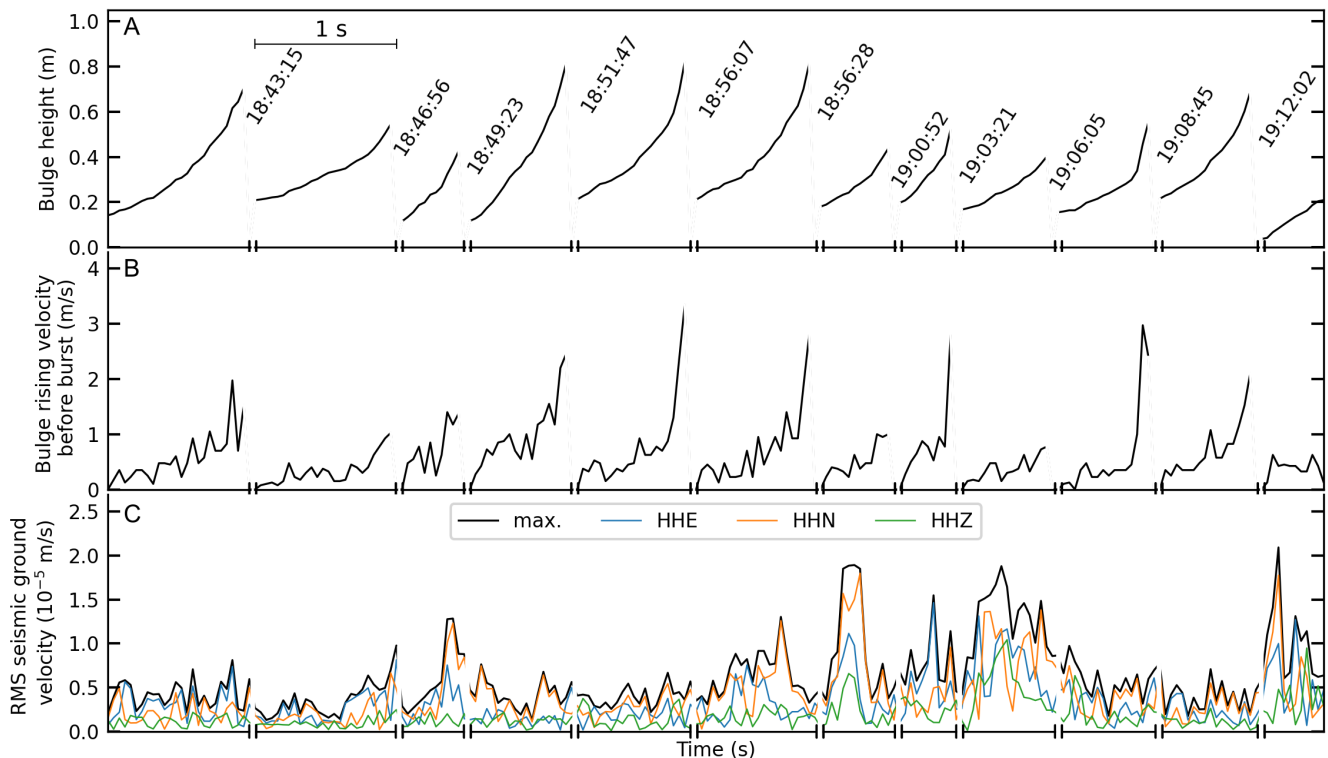


Figure 4: 11 bulges grow within less than 1.28 s on 13 March 2021. Evolution of [A] bulge height once a reliable measurement above the reference level is possible, [B] bulge rising velocity, and [C] RMS seismic ground velocity filtered from 3 to 30 Hz at station GE2. Note the time gaps of seconds to minutes marked by the broken x axis. The time is the time before the bulge bursts.

4.5 Jet heights and waiting time after single and double eruptions correlate

We separated the 67 maximum jet heights into single and double eruptions for the 2017 dataset. The water ejected during single eruptions reaches jet heights from 1.3 to 42.8 m and average jet heights of 21.1 ± 10.2 m. There is no clear trend in the distribution of jet heights and the following waiting time after the eruption (black dots in Figure 6A).

The first jet in double eruptions reaches heights from 6.4 to 48.1 m, while the second jet in double eruptions reaches heights from 6.3 to 41.7 m. The mean heights are 24.5 ± 14.3 m and 24.9 ± 13.0 m for the first and second jets, respectively. These means are comparable, although the standard deviation is larger for the height of the first jet (grey dots in Figure 6A). Compared to single eruptions, the mean jet heights for double eruptions are larger. Three out of seven double eruptions produce jets higher than 35 m and are among the highest observed. However, six out of 45 single eruptions also reach more than 35 m in height. While a large jet height can be reached in both single and double eruptions, it may be slightly more likely that a large jet is quickly followed by a second jet, making it typical of a double eruption.

In double eruptions, the first jet is smaller than the second in four out of seven cases. The second jet in double eruptions was smaller in one double eruption, and in two eruptions we only have a height measurement of one of the two jets (grey

dots in Figure 6A). A larger dataset is needed for robust statistical analysis.

We observed that the smallest first jet of a double eruption reached a height of only 6.5 m and was followed by a 0.18 min pause until the next jet. The largest first jet of a double eruption reached a height of 44.7 m and was followed by a pause of 0.27 min until the next jet. As the height of the first jet in a double eruption increases, the waiting time for the second jet in a double eruption increases (grey dots in Figure 6A).

A similar trend was found for the second jet in double eruptions. The smallest second jet reached a height of 10.9 m followed by a pause of 3.88 min until the next jet. The largest second jet reached a height of 41.7 m followed by a 7.1 min pause until the next jet (grey dots in Figure 6A). Larger second jets in a double eruption thus seem to cause longer waiting times before the next eruption.

We extracted the seismic amplitude at the time of maximum jet height (Figure 6B). The mean seismic ground velocity amplitude associated with the first and second jets in double eruptions is $0.55 \pm 0.16 \cdot 10^{-7}$ m s⁻¹ and $0.75 \pm 0.35 \cdot 10^{-7}$ m s⁻¹, respectively. This is slightly smaller than the mean seismic amplitude of $0.71 \pm 0.48 \cdot 10^{-7}$ m s⁻¹ observed for single eruptions. In two double eruptions, the seismic amplitudes associated with both jets are comparable, while in two cases the seismic amplitude during the second jet is larger.

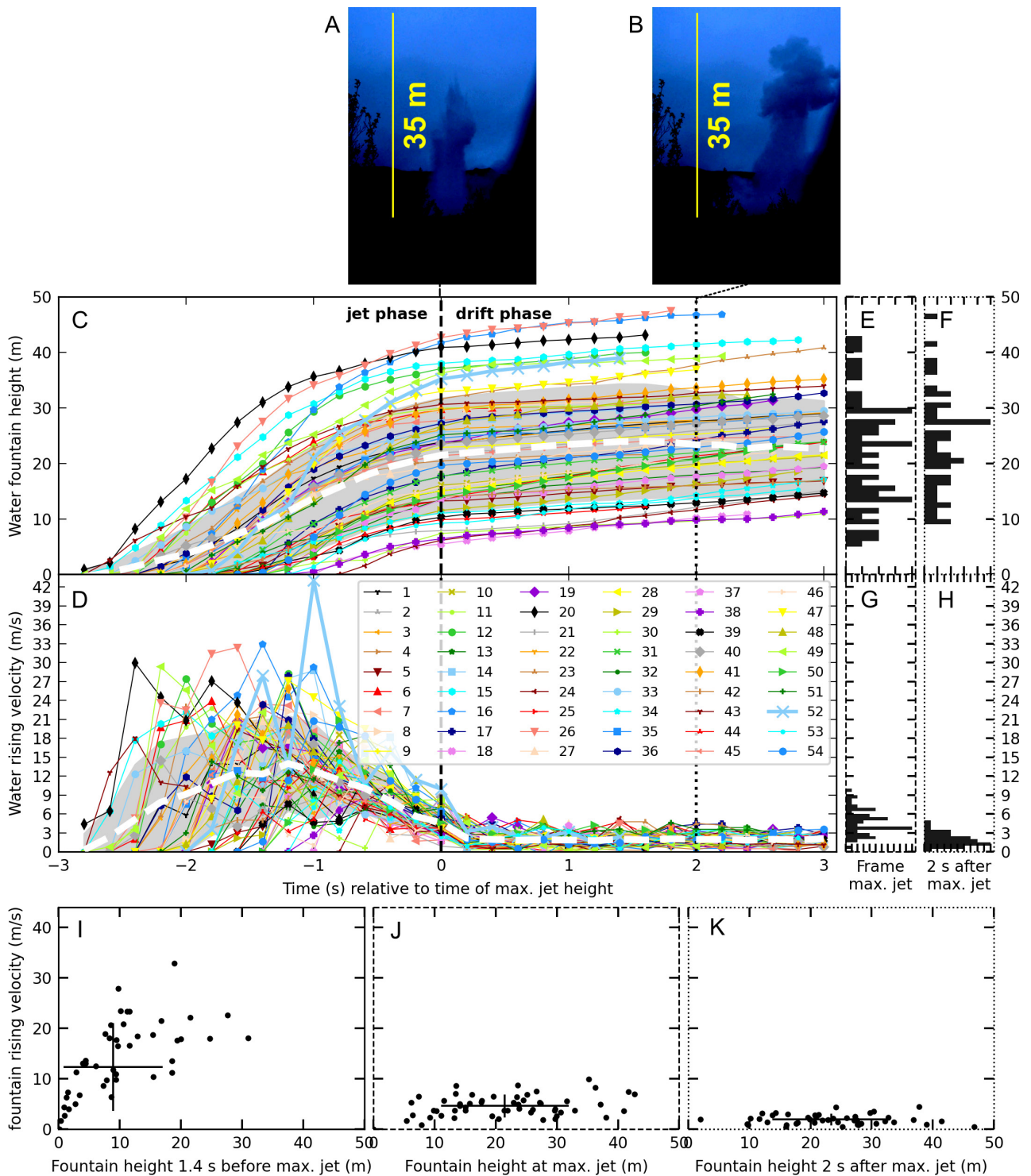


Figure 5: Water fountain heights and velocities from 27 to 30 June 2017. [A] Photos at maximum jet height and [B] drift height 2 s after maximum jet height. [C] Stacked height and [D] velocity for both jet and drift stages. The vertical dashed line indicates the time of maximum jet height and the dotted line the drift height reached 2 s later. [E]–[H] Histogram of [E] maximum jet height, [F] drift height 2 s after maximum jet height, [G] velocity at maximum jet height and [H] drift velocity 2 s after maximum jet height. White dashed lines and grey shaded areas like in Figure 2. [I]–[K] Fountain height vs. fountain rising velocity [I] 1.4 s before maximum jet height, [J] at maximum jet height and [K] 2 s after maximum jet height. Mean values \pm one standard deviation are highlighted with black bars.

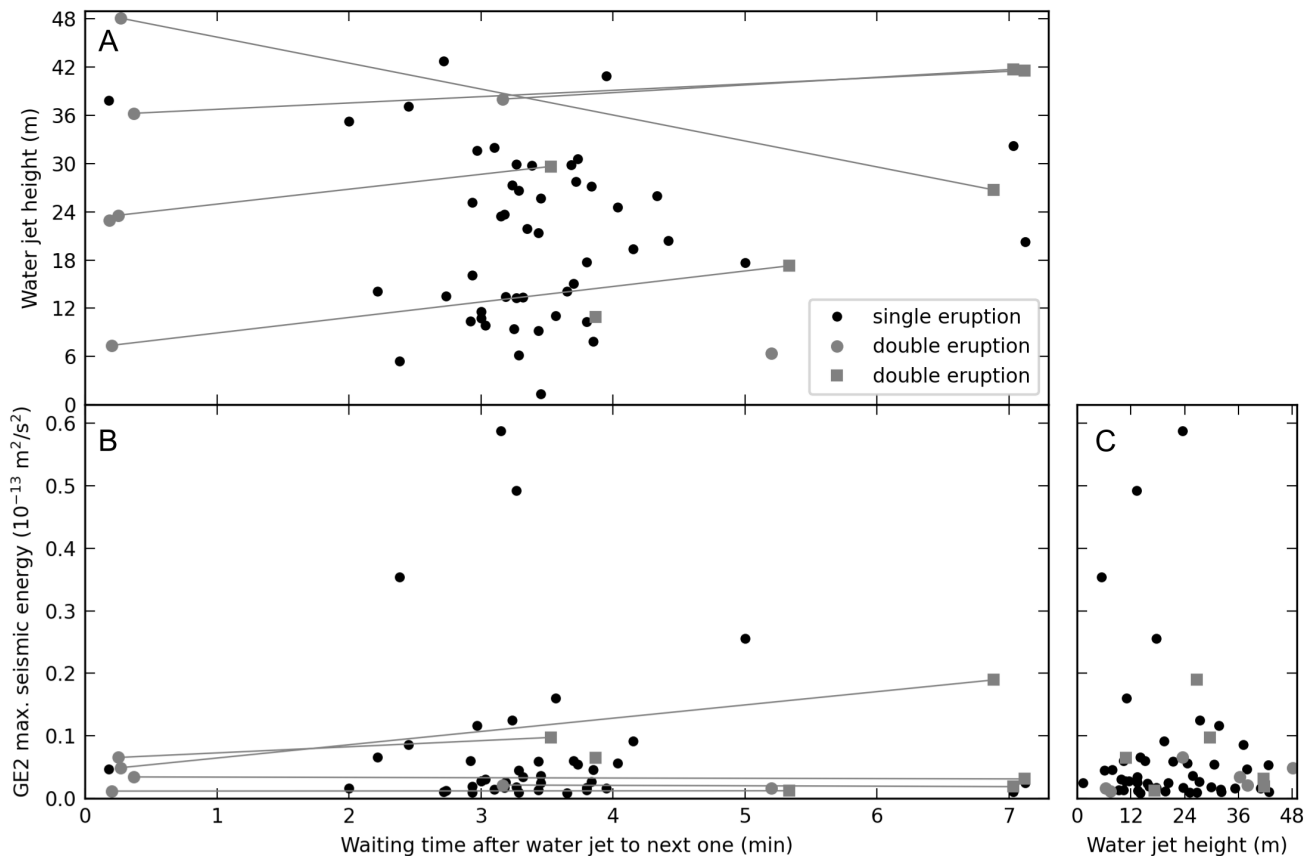


Figure 6: Link between eruption height and waiting time from 27 to 30 June 2017. [A] Jet eruption height in comparison with the following waiting time after the eruption. Colors indicate single (black) and double eruptions (grey). Dots indicate the first jets, while squares indicate the second jets in a double eruption. Jets belonging to the same double eruption are connected with a line. [B] Maximum seismic amplitudes associated with the following waiting time. [C] Maximum seismic amplitudes vs. the water jet height.

4.6 Jet heights and seismic energy are anti-correlated

The maximum measured ground motion in velocity is similar for GE2, GE3, and GE4 in 2017. The jets can also affect the three components of a seismometer differently, depending on the direction and location of the jet. We therefore compare the jet heights with the maximum seismic amplitude squared i.e. the maximum seismic energy.

Jet height is weakly anticorrelated with seismic amplitude with a Pearson correlation coefficient of -0.1 . Larger seismic energies are recorded during small eruptions, and large jets are associated with small seismic energies (Figure 6C and 7). However, small jets can be associated with both small and large seismic energies, and small seismic energies can be associated with both small and large jets. The correlation is therefore not strong (Figure 6C).

5 INTERPRETATION AND DISCUSSION

5.1 Limitations of the derived heights and velocities

This is the first attempt to analyze the dynamics and behavior of the developing geyser water bulge, and to compare its properties with seismic and jet height records. We used data collected in 2017, 2020, and 2022, which provide a robust

overview but also have some limitations that need to be discussed.

Our video recordings lack information necessary for accurate pixel-to-meter conversions. In particular, for the 2017 and 2022 datasets, camera height above ground, camera tilt angle, and recording time are poorly constrained and may have affected our results.

To address the issue of proper scaling of the 2017 and 2022 datasets, we used morphological features (outer conduit rims visible above the water surface) as a scaling reference. Measurements of these features were based on drone-based orthophoto mosaic results and photogrammetric data [Walter et al. 2020; Walter 2024]. The measurement results show a good correlation with the scaling information obtained in 2020 using a reference pole. There is also the possibility to calculate the image scaling factor from the camera parameters (such as focal length, pixel size, and known distance of the camera from the surveyed object). However, this technique can be applied to the original photographs but not to the video frames extracted with the different parameters. In addition, the precise distances from the camera to the Strokkur conduit are unknown for the 2017 and 2022 datasets. Regarding parameters such as camera height and tilt angle, we consider them not significant enough to cause noticeable distortion in the image

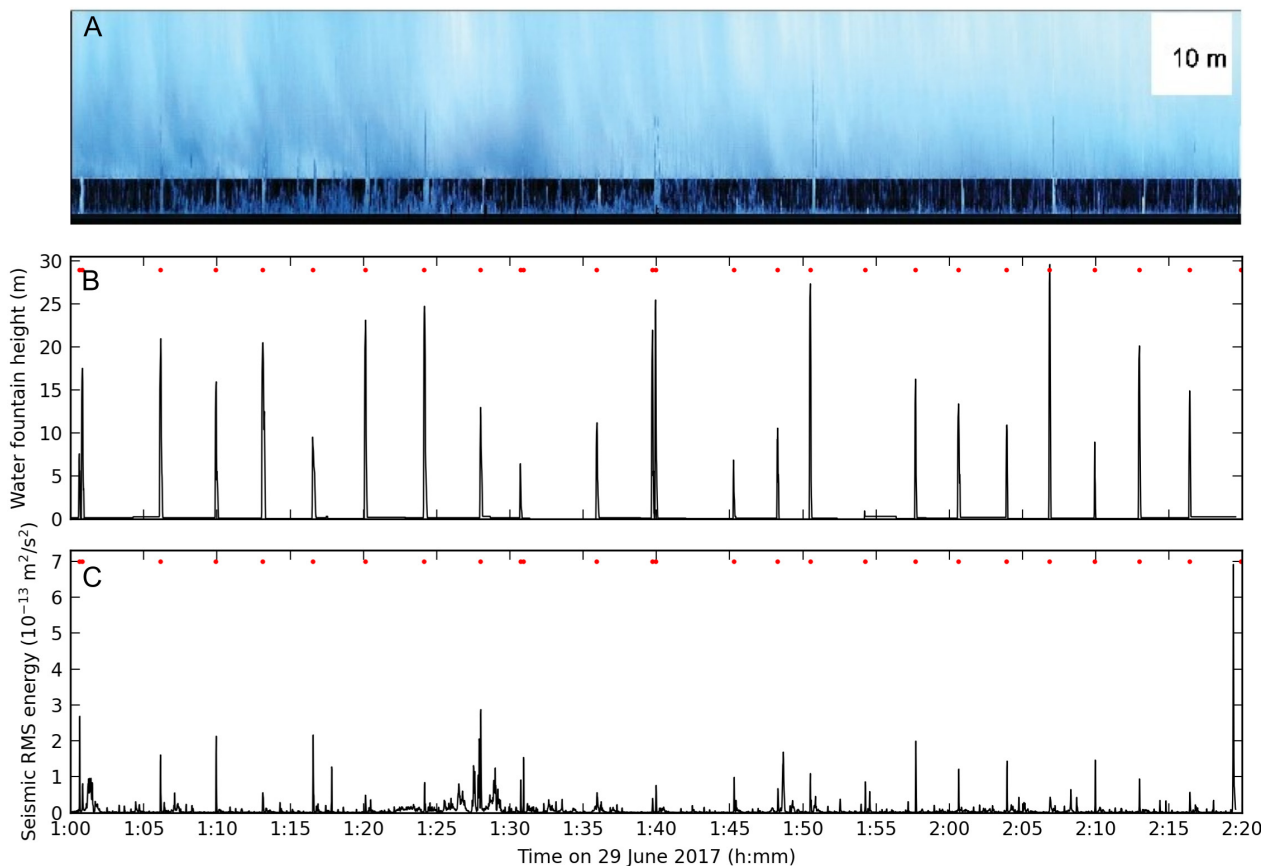


Figure 7: Eruption height estimated from video camera on 29 June 2017. [A] Kymograph time-slice showing the occurrence of eruptions (vertical axis) on a time axis (horizontal). [B] Comparison of events recorded from the kymograph slide to the [C] seismic energy. RMS of seismic recordings at G4 filtered 1 to 40 Hz calculated in 2 s long time windows with 50 % overlap. Red dots mark eruption marker from [Eibl et al. 2020a].

center region (around the bulge), although they should be considered for the jet measurements due to the much larger height of the object.

The 2020 dataset was collected at low air temperatures, which caused steam emissions and sometimes blurred the view of the bulge. Therefore, the bulge height estimate is more reliable when the wind is stronger because it blew the steam away. During our field campaigns we faced wind speeds of 3.5 to 5 m s⁻¹ according to a nearby weather station in Hjarðarland maintained by the Icelandic Meteorological Office. On both days in March it was comparable and most likely does not cause any bias in the bulge height. While a stronger wind could improve the visibility of the bulge, it could also reduce the height of the bulge, jet and the drifting cloud.

During our jet measurements in 2017, the wind speeds were less than 2 m s⁻¹ on the first two days and less than 2.8 m s⁻¹ on the third day. Therefore, our jet height measurements are comparable and not affected by different wind conditions. However, on some days we had clouds in the background, which made it difficult to track the jet height. In the future, the steam problem may be solved by using an infrared camera that would capture the clear boundary between the hot water bulge and the jet.

The available time resolution of the camera is not high enough to capture the maximum height of such an instantaneously developing water bulge. In the last frame before a bulge burst, the bulge is less than 0.04 s from the actual burst. If we catch it early, the velocity and height will be lower. Using a higher resolution camera and better timing the bulge bursts would slightly increase the average heights and velocities. But these values would still be within the one standard deviation we derived.

Since cameras with different fps were used, it was difficult to combine the datasets, e.g. to calculate the mean heights of the bulges. The differences in the mean values of 2020 and 2022 in Figure 2 are about 0.01 m and much smaller than one standard deviation of the bulge heights.

5.2 Velocities of the bubbles, bulge, and jet

The surface of the basin is pushed upward by the rising bubble with increasing velocity. We derive rising bubble velocities that increase from 0.9±0.5 m s⁻¹ to 2.3±1.1 m s⁻¹ in the frame before the bubble bursts. Collignon et al. [2023] measured at Strokkur in 2018, a velocity of 1 to 4 m s⁻¹ in the frame before the bulge bursts. They studied 14 bulges with a high speed camera. These velocities are consistent with our

findings, and therefore also give confidence that our camera records are properly scaled.

Assuming that these velocities represent the rising velocity of the steam bubble in the conduit, the bubble will accelerate as it reaches the surface. Thus, the bubble could initially rise at about 0.9 m s^{-1} and increase as the pressure drop escalates the conversion to steam and increases the bubble size.

We estimate the bubble's rising velocity u using Davies and Taylor's formula for isolated, large bubbles [Davies and Taylor 1950], assuming that the bubble's diameter, and therefore its rising velocity, does not increase as it rises: $u = 0.707 \cdot \sqrt{g \cdot l}$, where g is the acceleration due to gravity and l is the bubble diameter. A bubble rising at 1 m s^{-1} would be 0.2 m wide. For a bubble of 1 m in diameter we get a rise velocity of 2.2 m s^{-1} and a bubble filling the 2.2 m -wide conduit [Walter et al. 2020] can feature a velocity of 3.3 m s^{-1} . The upper limit of the velocities we reported might hence be limited by the diameter of the conduit whilst smaller velocities might indicate smaller bubbles. The equation assumes an isolated bubble in a large volume of fluid while our bubbles are confined in a conduit and are affected by free-surface frictional effects. We note (i) that the conduit is narrowing with depth and shaped rather elliptically in plane view, (ii) that rising bubbles coalesce and expand, and (iii) that the bubbles might be vertically elongated such as in slug flows so that the suggested values are highly conservative. For more discussion around slug flow, the dynamics of a wake of recirculating water following it at Strokkur, the reader is referred to Collignon et al. [2023].

Bubble rising velocities have been studied in various experimental setups, e.g. Jaupart and Vergnolle [1988, 1989] and Talaia [2007], using water, silicone oil, or glycerol. However, since the velocity depends on the size and properties of the fluid, a detailed discussion of velocities in other contexts seems inappropriate. Once the bulge bursts, the velocity at Strokkur peaks with an average maximum jet velocity of $14.0 \pm 7.5 \text{ m s}^{-1}$. For water fountains, maximum velocities of 10 to 28 m s^{-1} have been observed at Lone Star Geyser, USA [Karlstrom et al. 2013]. Their reported jet width at the lower 30 cm was only 0.79 m . Here we observed higher jet velocities up to 44 m s^{-1} associated with a wider jet fed by bulges with mean widths of $2.65 \pm 0.13 \text{ m}$. Rudolph et al. [2012] reported maximum exit velocities of 10 to 20 m s^{-1} at Calistoga Geyser, USA, which are comparable to our jet velocity values.

5.3 The bubble path and its rising velocity

In stage (iv) of the eruptive cycle, bubbles burst at depth at intervals of 27 to 20 s [Eibl et al. 2021]. Assuming a velocity of 2.2 m s^{-1} , the distance traveled would be 44 to 59.4 m . The vertical part of the conduit is about 25 m long and the horizontal distance from the conduit to the bubble trap is 13 m [Eibl et al. 2021] yielding a likely bubble path of 38 m length. Bubbles hence likely travel at less than 2.2 m s^{-1} average speed. This might either indicate significantly slower speeds in the horizontal part of the conduit or overall smaller velocities due to friction, non-circular bubble shapes or smaller bubble sizes. A bubble with a smaller radius is likely at this stage of the eruptive cycle, and given that the initial bulge rising velocities we observe at the surface are around 0.1 m s^{-1} .

A decreasing time interval between bubble bursts at depth within stage (iv) may reflect increasing ascent velocities as the bubbles grow. In the horizontal part of the conduit, the velocity is probably slower, but it remains an open question whether bubbles are released near the bubble trap or only when they reach the vertical part of the conduit. In the latter case, we can ignore the horizontal distance traveled, and the temporal spacing of the bubble bursts provides a measure of the bubble velocity in the conduit as described above.

5.4 Bulge height and fountain height

We observed bulge heights of $0.62 \pm 0.18 \text{ m}$. We found that smaller bulges grow more slowly. Assuming a constant rate at which the displaced layer of water flows back to the bottom, a slower rate of ascent will result in a smaller bulge at the time of the eruption. The single eruptions include both the smallest and the largest bulges, and thus show the largest variations, perhaps due to incomplete coalescence in the conduit. However, as a bubble rises and reaches the surface, all bulges begin to grow at a slow rate. So the difference between fast rising high bulge and slow rising smaller bulge may be that the still-slow-rising bulges do not have time to increase in speed and height. Instead, they reach bursting conditions too early and create only a small bulge. Consequently, a small bulge will result in a small eruption jet height. We speculate that either there is less energy available in the rising steam bubble, or the available energy is not efficiently channeled to form a large vertical jet, but is instead lost horizontally into the earth.

Barth [1940] reported failed eruptions at Great Geysir, Iceland, and that eruptions are not regular in height and frequency. Here we reported jet heights ranging from 5.4 to 42.8 m , but we also visually observed jets as low as 1 m at the site. We observed average jet heights of $21.4 \pm 10.2 \text{ m}$. At Lone Star, Karlstrom et al. [2013] reported a maximum fountain height of just over 12.8 m . Munoz-Saez et al. [2015] reported maximum heights of 2 m at El Jefe geyser, Chile. Studies of Yellowstone geysers in the Upper Geyser Basin, Lower Geyser Basin, and Norris Geyser Basin suggest that reservoir depth may be a major determinant of eruption height, with deeper reservoirs resulting in higher eruption velocities and more impulsive and taller geyser eruptions [Reed et al. 2021]. This tendency for geysers with deeper water sources to have higher eruptions is explained by an isentropically expanding water source. According to the relation derived in Reed et al. [2021] and the average 21.4 m -high jets observed at Strokkur, we could infer a bubble reservoir at 11 m depth. However, according to Eibl et al. [2021], the seismic data suggest a bubble trap at $23.7 \pm 4.4 \text{ m}$ depth. Thus, their proposed model underestimates the depth of the bubble trap in our case. However, their model is also based on a data point from Strokkur at 30 m fountain height and 13 m reservoir depth. The values they used to build their model are therefore not consistent with the heights derived here and the depths derived by Eibl et al. [2021].

5.5 Seismic amplitude and height

We observed that the six highest jets produce low seismic amplitudes of less than $0.8 \cdot 10^{-7} \text{ m s}^{-1}$ and that the six largest

seismic amplitudes are associated with eruptions of less than 28 m-high jets. However, neither small seismic amplitudes nor small jet heights could be reliably interpreted in the context of jet height and seismic amplitude, respectively. We speculate that the bubble slug couples more effectively to the conduit walls in small eruptions due to a slower rising velocity or less bubble foam. This better coupling could be reflected in larger amplitudes. In large eruptions, water is ejected into the air more quickly and may be surrounded by more bubbles that attenuate the seismic signal.

We noticed that some bubbles burst at about 1 m depth. They most likely reached unfavorable conditions that triggered the burst. The energy is then released sideways into the earth, creating a very small jet. This could cause a larger seismic amplitude.

6 CONCLUSION AND OUTLOOK

Strokkur is an active geyser erupting every 3.7 to 16.4 min [Eibl et al. 2020a]. We combined analysis of video camera data with seismic data to assess the relationship between observed ground motion, bulge, and jet heights. The eruption begins with the formation of a blue bulge that has an average width of 2.65 ± 0.13 m and a height of 0.62 ± 0.18 m in the pre-burst frame. In this frame, it rises at an average velocity of 2.3 ± 1.1 m s⁻¹ and takes an average of 0.74 ± 0.27 s to form. When the bulge bursts, a jet forms which reaches maximum height within 2.8 s. The average vertical velocity during the jet stage peaks at 14.0 ± 7.5 m s⁻¹ and drops to a stable 2.0 ± 1.0 m s⁻¹ during the drift stage. We find that larger bulges are associated with larger ascent velocities and larger jets are associated with larger jet velocities. In such cases, the energy released during the eruption is thus efficiently channeled into a large bulge and a large jet, while not generating much seismic ground motion. In contrast, larger jets are followed by a longer waiting time for the next one, and Collignon et al. [2023] confirmed that more energy is lost during large eruptions, which must be supplied by the heat source at depth at a possibly constant rate.

It is remarkable how regularly the eruptions at Strokkur produce blue water bulges before jetting into the air, given how rare this observation is at geysers worldwide. Bulges do not form at Strokkur if the bubble bursts too deep. In such a scenario, the rising bubble probably encountered water conditions that were too cold to maintain the bubble [Eibl et al. 2021], causing it to burst. In such a case, only splashes of water are visible on the surface. If similar unfavorable conditions can be maintained more long-term near the surface of other geysers, a rising bubble may never cause a blue bulge. However, one has to also keep in mind that the conduit geometries and underlying processes that maintain the jetting may differ, as eruptions at other geysers often last much longer than the few seconds at Strokkur. If these eruptions lead to a churned water surface, this may not allow bulge formation, but may trigger early bursts. What may be unique at Strokkur (and Great Geysir) is the nearly vertical conduit geometry [Walter et al. 2020] and the large deep bubble trap [Eibl et al. 2021], which allows bubbles to rise and expand undisturbed in a slug flow, pushing a large, homogeneous water bulge upward

at the surface prior to eruption. Further studies and experiments with conduit and pool geometries and sizes are needed for a definitive answer.

Our experiments at Strokkur over several years have shown that seismometers are a simple and reliable tool for monitoring the regularity of the geyser long-term and to illuminate geyser-related processes at depth. However, they are affected by anthropogenic or environmental noise when the geyser is visited by many tourists, when the instrument has to be placed far from the source, or when the instrument cannot be buried in the ground. Battery failure or increased power consumption of the sensors during periods of low temperature must be considered. At Strokkur, the seismic signal from the geyser decays fast due to its dominant frequency content of more than 3 Hz [Eibl et al. 2021] and is difficult to detect at a distance of more than 100 m. In addition, it is visited by up to 15,000 tourists per day (pers. comm. ranger in August 2023) and within 40 m distance most of the surface is sintered.

Video data have proven very useful in assessing the visual processes and their characteristics at the surface and in developing an understanding of the recorded seismic signals. However, we have faced a number of problems with the video data over the years, and things to consider are the power consumption of the camera in cold conditions, the time resolution required for fast evolving features, the camera position, viewing angle and scale, an accurate visual and acoustic signal for exact timing, the storage requirements for both high resolution images, and recordings of up to one minute to capture the dynamics of higher order eruptions. Of course, these requirements can escalate if a geyser is erupting for several minutes or hours. If the sound recording of the camera is to be analyzed, it should be placed closer to the geyser, sheltered from the wind, and no one should be talking on site.

In a future where these problems have been solved, we will ultimately face huge amounts of seismic and video data near geysers or volcanoes, which will need to be processed in an automated way to speed up the analysis we presented here. A statistically significant sample size will then form the basis of a detailed model describing the relationship between geyser behaviour and the seismic signal. Ultimately, our goal should be a total energy balance for the system. This includes the conversion of thermal energy that is stored mostly in the system liquids which have high heat capacity to mechanical energy. Vaporization of liquid to steam also consumes energy due to higher enthalpy of vapor relative to liquid. So the system loses energy, and the temperature of the fluids decreases whilst energy is converted into seismic energy, kinetic energy, and finally potential energy.

Our study contributes to a better understanding of seismic signals generated by bubble migration and bursting. We also shed light on the clear link between the size of the bubble and the following fountain. The used approaches and findings are relevant for volcanic systems where bubbles play an important role in driving effusive or explosive eruptions.

AUTHOR CONTRIBUTIONS

E.E., A.S. and T.W. organised the field work, collected the data and initiated the study. G.H. supported the field work. E.E.

analyzed and interpreted the seismic data and created eruption catalogs. S.K. analyzed the video footage and extracted heights and velocities with help from A.S. and T.W. A.S. estimated the bulge morphometry and T.W. calculated kymographs. E.E. led the writing of the manuscript with contributions from all authors.

ACKNOWLEDGEMENTS

We thank the Environment Agency of Iceland and the National Energy Authority for the research permit in the geothermal area around Strokkur. We thank the rangers for their guidance and support. The meteorological data was supplied by the Icelandic Meteorological Office, retrieved on 10 August 2021. This work was financially supported by the Daimler Benz Foundation (32-02/18). We thank Tanja Witt, Masoud Allahbakhshi, Magnus T. Gudmundsson, Alexander Belousov, Daniel Vollmer, Bergur H. Bergsson, Philippe Jousset, Torsten Dahm and Thoralf Dietrich for their support in the field.

DATA AVAILABILITY

The 2017/18 seismic data is available via GEOFON (network code 7L) [Eibl et al. 2020b]. We uploaded to GFZ Data Services the corresponding eruption marker file [Eibl et al. 2019], the drone data [Walter 2024] and the derived speed and height catalogs [Eibl et al. 2024]. Video data is available upon request.

COPYRIGHT NOTICE

© The Author(s) 2024. This article is distributed under the terms of the [Creative Commons Attribution 4.0 International License](https://creativecommons.org/licenses/by/4.0/), which permits unrestricted use, distribution, and reproduction in any medium, provided you give appropriate credit to the original author(s) and the source, provide a link to the Creative Commons license, and indicate if changes were made.

REFERENCES

- Alparone, S., D. Andronico, L. Lodato, and T. Sgroi (2003). “Relationship between tremor and volcanic activity during the Southeast Crater eruption on Mount Etna in early 2000”. *Journal of Geophysical Research: Solid Earth* 108(B5), pages 1–13. DOI: [10.1029/2002JB001866](https://doi.org/10.1029/2002JB001866).
- Arnórsson, S. (1985). “The use of mixing models and chemical geothermometers for estimating underground temperatures in geothermal systems”. *Journal of Volcanology and Geothermal Research* 23(3–4), pages 299–335. DOI: [10.1016/0377-0273\(85\)90039-3](https://doi.org/10.1016/0377-0273(85)90039-3).
- Barth, T. F. W. (1940). “Geysir in Iceland”. *American Journal of Science* 238(6), pages 381–407.
- Bouche, E., S. Vergnolle, T. Staudacher, A. Nercessian, J.-C. Delmont, M. Frogneux, F. Cartault, and A. Le Pichon (2010). “The role of large bubbles detected from acoustic measurements on the dynamics of Erta 'Ale lava lake (Ethiopia)”. *Earth and Planetary Science Letters* 295(1), pages 37–48. DOI: <https://doi.org/10.1016/j.epsl.2010.03.020>.
- Bryan, T. S. (2008). *The geysers of Yellowstone*. University press of Colorado.
- Bunsen, R. (1847). “Über den inneren Zusammenhang der pseudovulkanischen Erscheinungen Islands”. *Wöhlers und Liebigs Annalen der Chemie und Pharmacie* LXII, pages 1–59.
- Collignon, M., L. Pioli, D. Trippanera, A. Carrier, and M. Lupi (2023). “Conduit Processes at the Haukadalur Geyser-Hosting Hydrothermal Field (Iceland) Revealed by In Situ Temperature and High-Speed Camera Measurements”. *Journal of Geophysical Research: Solid Earth* 128(11). DOI: [10.1029/2022jb026140](https://doi.org/10.1029/2022jb026140).
- Davies, R. M. and G. I. Taylor (1950). “The mechanics of large bubbles rising through extended liquids and through liquids in tubes”. *Proceedings of the Royal Society of London A: Mathematical, Physical and Engineering Sciences* 200(1062), pages 375–390. DOI: [10.1098/rspa.1950.0023](https://doi.org/10.1098/rspa.1950.0023).
- Descloizeaux, A. (1847). “LX. Physical and geological observations on the principal Geysirs of Iceland”. *The London, Edinburgh, and Dublin Philosophical Magazine and Journal of Science* 30(203), pages 391–409. DOI: [10.1080/14786444708645417](https://doi.org/10.1080/14786444708645417).
- Edwards, M. J., B. M. Kennedy, A. D. Jolly, B. Scheu, and P. Jousset (2017). “Evolution of a small hydrothermal eruption episode through a mud pool of varying depth and rheology, White Island, NZ”. *Bulletin of Volcanology* 79(2). DOI: [10.1007/s00445-017-1100-5](https://doi.org/10.1007/s00445-017-1100-5).
- Eibl, E. P. S., S. Hainzl, N. I. K. Vesely, T. R. Walter, P. Jousset, G. P. Hersir, and T. Dahm (2020a). “Eruption Interval Monitoring at Strokkur Geyser, Iceland”. *Geophysical Research Letters* 47(1). DOI: [10.1029/2019gl085266](https://doi.org/10.1029/2019gl085266).
- Eibl, E. P. S., P. Jousset, T. Dahm, T. R. Walter, G. P. Hersir, and N. I. K. Vesely (2019). “Seismic experiment at the Strokkur Geyser, Iceland, allows to derive a catalogue of over 70,000 eruptions.” *GFZ Data Services*. DOI: [10.5880/GFZ.2.1.2019.005](https://doi.org/10.5880/GFZ.2.1.2019.005).
- Eibl, E. P. S., S. Karmacharya, A. V. Shevchenko, T. R. Walter, and G. P. Hersir (2024). “Catalogues of bulge and fountain formation at Strokkur geyser in 2017, 2020 and 2022: Heights, rising speeds and seismic signal”. *GFZ Data Services*. DOI: [10.5880/fidgeo.2024.010](https://doi.org/10.5880/fidgeo.2024.010).
- Eibl, E. P. S., D. Müller, T. R. Walter, M. Allahbakhshi, P. Jousset, G. P. Hersir, and T. Dahm (2021). “Eruptive Cycle and Bubble Trap of Strokkur Geyser, Iceland”. *Journal of Geophysical Research: Solid Earth* 126(4). DOI: [10.1029/2020JB020769](https://doi.org/10.1029/2020JB020769).
- Eibl, E. P. S., T. Thordarson, Á. Höskuldsson, E. Á. Gudnason, T. Dietrich, G. P. Hersir, and T. Ágústsdóttir (2023). “Evolving shallow conduit revealed by tremor and vent activity observations during episodic lava fountaining of the 2021 Geldingadalir eruption, Iceland”. *Bulletin of Volcanology* 85(2). DOI: [10.1007/s00445-022-01622-z](https://doi.org/10.1007/s00445-022-01622-z).
- Eibl, E. P. S., T. Walter, P. Jousset, T. Dahm, M. Allahbakhshi, D. Müller, and G. Hersir (2020b). “1 year seismological experiment at Strokkur in 2017/18”. *GFZ Data Services. Other/Seismic Network*. DOI: [10.14470/2Y7562610816](https://doi.org/10.14470/2Y7562610816).
- Heimann, S., M. Kriegerowski, M. Isken, S. Cesca, S. Daout, F. Grigoli, C. Juretzek, T. Megies, N. Nooshiri, A. Steinberg, H. Sudhaus, H. Vasyura-Bathke, T. Willey, and T. Dahm (2017). *Pyrocko - An open-source seismology toolbox and library. V. 0.3*. Technical report. GFZ. DOI: [10.5880/GFZ.2.1.2017.001](https://doi.org/10.5880/GFZ.2.1.2017.001).

- Hovland, M., A. Hill, and D. Stokes (1997). “The structure and geomorphology of the Dashgil mud volcano, Azerbaijan”. *Geomorphology* 21(1), pages 1–15. DOI: [10.1016/S0169-555X\(97\)00034-2](https://doi.org/10.1016/S0169-555X(97)00034-2).
- Hurwitz, S. and M. Manga (2017). “The Fascinating and Complex Dynamics of Geyser Eruptions”. *Annual Review of Earth and Planetary Sciences* 45(1), pages 31–59. DOI: [10.1146/annurev-earth-063016-015605](https://doi.org/10.1146/annurev-earth-063016-015605).
- Hurwitz, S., M. Manga, K. Campbell, C. Muñoz-Saez, and E. P. S. Eibl (2021). “Why Study Geysers?” *Eos* 102. DOI: [10.1029/2021eo161365](https://doi.org/10.1029/2021eo161365).
- Hurwitz, S. and D. R. Shelly (2017). “Illuminating the Voluminous Subsurface Structures of Old Faithful Geyser, Yellowstone National Park”. *Geophysical Research Letters* 44(20), pages 10, 328–10, 331. DOI: [10.1002/2017GL075833](https://doi.org/10.1002/2017GL075833).
- Hutchinson, R. A., J. A. Westphal, and S. W. Kieffer (1997). “In situ observations of Old Faithful Geyser”. *Geology* 25(10), pages 875–878. DOI: [10.1130/0091-7613\(1997\)025<0875:IS000F>2.3.CO;2](https://doi.org/10.1130/0091-7613(1997)025<0875:IS000F>2.3.CO;2).
- Jaupart, C. and S. Vergnolle (1988). “Laboratory models of Hawaiian and Strombolian eruptions”. *Nature* 331(6151), pages 58–60. DOI: [10.1038/331058a0](https://doi.org/10.1038/331058a0).
- (1989). “The Generation and Collapse of a foam Layer at the Roof of a Basaltic Magma Chamber”. *Journal of Fluid Mechanics* 203(347), pages 347–380. DOI: [10.1017/S0022112089001497](https://doi.org/10.1017/S0022112089001497).
- Jones, B., R. W. Renaut, H. Torfason, and R. B. Owen (2007). “The geological history of Geysir, Iceland: A tephrochronological approach to the dating of sinter”. *Journal of the Geological Society* 164(6), pages 1241–1252. DOI: [10.1144/0016-76492006-178](https://doi.org/10.1144/0016-76492006-178).
- Karlstrom, L., S. Hurwitz, R. Sohn, J. Vandemeulebrouck, F. Murphy, M. L. Rudolph, M. J. Johnston, M. Manga, and R. B. McCleskey (2013). “Eruptions at Lone Star Geyser, Yellowstone National Park, USA: 1. Energetics and eruption dynamics”. *Journal of Geophysical Research: Solid Earth* 118(8), pages 4048–4062. DOI: [10.1002/jgrb.50251](https://doi.org/10.1002/jgrb.50251).
- Keller, J. and M. Krafft (1990). “Effusive natrocarbonatite activity of Oldoinyo Lengai, June 1988”. *Bulletin of Volcanology* 52(8), pages 629–645. DOI: [10.1007/BF00301213](https://doi.org/10.1007/BF00301213).
- Koyanagi, R. Y., B. A. Chouet, and K. Aki (1987). “Origin of volcanic tremor in Hawaii, part I. Data from the Hawaiian Volcano Observatory, 1969-1985”. *U.S. Geological Survey Professional Paper 1350*. Edited by R. W. Decker, T. W. Wright, and P. H. Stauffer. Volume v. 2. U.S. Geol. Surv. Prof. Pap., 1350, p. 1221–1257.
- MacKenzie, G. (1811). *Voyage to the Island of Iceland in the Summer of 1810*. Technical report, page 228.
- McNutt, S. R. (1987). “Volcanic tremor at Pavlof Volcano, Alaska, October 1973-April 1986”. *Pure and Applied Geophysics PAGEOPH* 125(6), pages 1051–1077. DOI: [10.1007/BF00879368](https://doi.org/10.1007/BF00879368).
- Meijering, E., O. Dzyubachyk, and I. Smal (2012). “Methods for cell and particle tracking.” *Methods in enzymology* 504, pages 183–200. DOI: [10.1016/B978-0-12-391857-4.00009-4](https://doi.org/10.1016/B978-0-12-391857-4.00009-4).
- Munoz-Saez, C., M. Manga, S. Hurwitz, M. L. Rudolph, A. Namiki, and C. Y. Wang (2015). “Dynamics within geyser conduits, and sensitivity to environmental perturbations: Insights from a periodic geyser in the El Tatio geyser field, Atacama Desert, Chile”. *Journal of Volcanology and Geothermal Research* 292, pages 41–55. DOI: [10.1016/j.jvolgeores.2015.01.002](https://doi.org/10.1016/j.jvolgeores.2015.01.002).
- Namiki, A., C. Muñoz-Saez, and M. Manga (2014). “El Cobreloa: A geyser with two distinct eruption styles”. *Journal of Geophysical Research: Solid Earth* 119(8), pages 6229–6248. DOI: [10.1002/2014JB011009](https://doi.org/10.1002/2014JB011009).
- Nishimura, T., M. Ichihara, and S. Ueki (2006). “Investigation of the Onikobe geyser, NE Japan, by observing the ground tilt and flow parameters”. *Earth, Planets and Space* 58(6), e21–e24. DOI: [10.1186/bf03351967](https://doi.org/10.1186/bf03351967).
- Ohlsen, L. O. (1805). “Om vandspringene Geiser og Strok i Island”. *Vid. Selsk. Skrifter IV, I*, 235–247. (in Danish).
- Ólafsson, Þ. (1967). “Rennslismælingar í Árnessýslu og Rangárvallasýslu í júní og júlí 1967”. *Orkustofnun, jarðhitadeild*, 28 pp (in Icelandic).
- Pálsson, S. (1983). *Ferðabók Sveins Pálssonar. Dagbækur og ritgerðir 1791-1797. I. og II. bindi. Örn og Örlygur*. Reykjavík.
- Pasvanoglu, S. (1998). “Geochemical Study of The Geyser Geothermal Field in Haukadalur, S-Iceland”. *Geothermal Training Programme* 11, pages 281–318.
- Pasvanoglu, S., H. Kristmannsdóttir, S. Björnsson, and H. Torfason (2000). “Geochemical Study of The Geyser Geothermal Field in Haukadalur, S-Iceland”. *Proceeding World Geothermal Congress 2000* (January), pages 675–680.
- Privitera, E., T. Sgroi, and S. Gresta (2003). “Statistical analysis of intermittent volcanic tremor associated with the September 1989 summit explosive eruptions at Mount Etna, Sicily”. *Journal of Volcanology and Geothermal Research* 120(3–4), pages 235–247. DOI: [10.1016/S0377-0273\(02\)00400-6](https://doi.org/10.1016/S0377-0273(02)00400-6).
- Quezada-Reyes, A. (2012). “Characterization of some Yellowstone geysers’ eruptions using infrasound”. PhD thesis. New Mexico Institute of Mining and Technology.
- Reed, M. H., C. Munoz-Saez, S. Hajimirza, S.-M. Wu, A. Barth, T. Girona, M. Rasht-Behesht, E. B. White, M. S. Karplus, S. Hurwitz, and M. Manga (2021). “The 2018 reawakening and eruption dynamics of Steamboat Geyser, the world’s tallest active geyser”. *Proceedings of the National Academy of Sciences* 118(2), e2020943118. DOI: [10.1073/pnas.2020943118](https://doi.org/10.1073/pnas.2020943118).
- Rinehart, J. S. (1968). “Seismic signatures of some Icelandic geysers”. *Journal of Geophysical Research* 73(14), pages 4609–4614. DOI: [10.1029/jb073i014p04609](https://doi.org/10.1029/jb073i014p04609).
- Rudolph, M. L., M. Manga, S. Hurwitz, M. Johnston, L. Karlstrom, and C. Y. Wang (2012). “Mechanics of old faithful Geyser, Calistoga, California”. *Geophysical Research Letters* 39(24), pages 1–5. DOI: [10.1029/2012GL054012](https://doi.org/10.1029/2012GL054012).
- Schindelin, J., I. Arganda-Carrera, E. Frise, K. Verena, L. Mark, P. Tobias, P. Stephan, R. Curtis, S. Stephan, S. Benjamin, T. Jean-Yves, J. W. Daniel, H. Volker, E. Kevin, T. Pavel, and C. Albert (2012). “Fiji - an Open platform for biological image analysis”. *Nature Methods* 9(7). DOI: [10.1038/nmeth.2019](https://doi.org/10.1038/nmeth.2019). Fiji.

- Talaia, M. A. R. (2007). "Terminal Velocity of a Bubble Rise in a Liquid Column". *International Journal of Physical and Mathematical Sciences* 1(4), pages 220–224. DOI: [10.5281/zenodo.1070173](https://doi.org/10.5281/zenodo.1070173).
- Tanguy, J. C. and G. Patané (1984). "Activity of mount Etna, 1977–1983: Volcanic phenomena and accompanying seismic tremor". *Bulletin Volcanologique* 47(4), pages 965–976. DOI: [10.1007/bf01952355](https://doi.org/10.1007/bf01952355).
- Torfason, H. (1995). *Strokkur (in Icelandic)*. Technical report. Reykjavik: Orkustofnun.
- Vergnolle, S. and G. Brandeis (1996). "Strombolian explosions: 1. A large bubble breaking at the surface of a lava column as a source of sound". *Journal of Geophysical Research: Solid Earth* 101(B9), pages 20433–20447. DOI: [10.1029/96jb01178](https://doi.org/10.1029/96jb01178).
- Walter, T. R. (2024). "Drone based photogrammetry data at the Geysir geothermal field, Iceland". *GFZ Data Services*. DOI: [10.5880/GFZ.2.1.2024.001](https://doi.org/10.5880/GFZ.2.1.2024.001). [Dataset].
- Walter, T. R., P. Jousset, M. Allahbakhshi, T. Witt, M. T. Gudmundsson, and P. Hersir (2020). "Underwater and drone based photogrammetry reveals structural control at Geysir geothermal field in Iceland". *Journal of Volcanology and Geothermal Research* 391(106282). DOI: [10.1016/j.jvolgeores.2018.01.010](https://doi.org/10.1016/j.jvolgeores.2018.01.010).
- Zhang, J. Y., C. Yan, and X. X. Huang (2009). "Edge detection of images based on improved sobel operator and genetic algorithms". *Proceedings of 2009 International Conference on Image Analysis and Signal Processing, IASP 2009*, pages 32–35. ISBN: 9781424439867. DOI: [10.1109/IASP.2009.5054605](https://doi.org/10.1109/IASP.2009.5054605).

7 APPENDIX

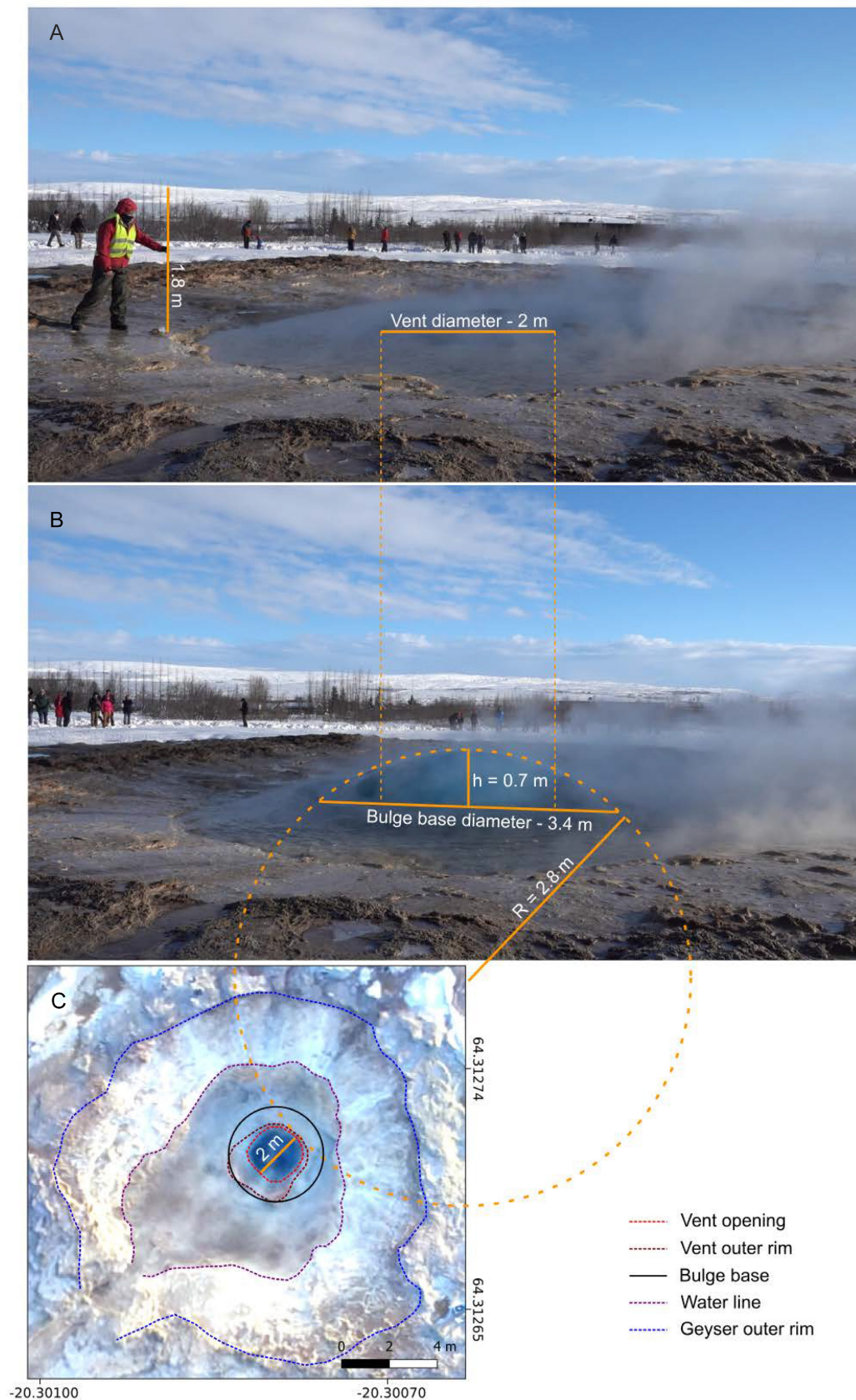


Figure S1: Measurements of the bulge morphometric parameters: [A] Video frame with a pole that was used as a reference. [B] Video frame that was used for the bulge measurements. [C] Drone-based orthophoto map of Strokkur that was used for the measurement validation.